

1 **Porosity-Permeability Relationships in Mudstone from Pore-Scale Fluid Flow Simulations using the**
2 **Lattice Boltzmann Method**

3 **Harsh Biren Vora¹, Brandon Dugan²**

4 ¹Department of Earth, Environment and Planetary Sciences, Rice University, Houston, TX 77005

5 ²Department of Geophysics, Colorado School of Mines, Golden, CO 80401

6 Corresponding Author: Harsh Biren Vora (hv6@rice.edu)

7 **Key Points:**

- 8 • We develop a model to predict mudstone permeability from clay platelet geometry using lattice
9 Boltzmann simulations
- 10 • Modeled porosity-permeability predictions match experimental observations from synthetic and
11 natural mudstones
- 12 • Our model can simulate mudstone permeability response to compaction and to fluid injection
13 using porosity and clay mineralogy

Abstract

We model mudstone permeability during consolidation and grain rotation, and during fluid injection by simulating porous media flow using the lattice Boltzmann method. We define the mudstone structure using clay platelet thickness, aspect ratio, orientation and pore widths. Over the representative range of clay platelet lengths (0.1–3 μm), aspect ratios (length/thickness=20–50) and porosities ($\phi=0.07$ –0.80) our permeability results match mudstone datasets well. Homogenous smectite and kaolinite models document a log-linear decline in vertical permeability from $8.31 \times 10^{-15} \text{ m}^2$ – $6.84 \times 10^{-17} \text{ m}^2$ at $\phi=0.73$ –0.80 to $6.33 \times 10^{-19} \text{ m}^2$ – $1.30 \times 10^{-23} \text{ m}^2$ at $\phi=0.07$ –0.16, showing good correlation with experimental data ($R^2=0.42$ and 0.56). We employ our methodology to predict the permeability of two natural mudstone samples composed of smectite, illite, and chlorite grains. Over $\phi=0.32$ –0.58, the permeability trends of two models replicating the mineralogical composition of the natural mudstone samples match experimental datasets well ($R^2=0.78$ and 0.74). We extend our methodology to evaluate how vertical mudstone permeability might evolve during microfracture network growth or macrofracture propagation upon fluid injection. Fluid injection results in a permeability increase from $1.02 \times 10^{-20} \text{ m}^2$ at $\phi=0.07$ to $2.07 \times 10^{-16} \text{ m}^2$ at $\phi=0.29$ for growth of a microfracture network, and from $1.02 \times 10^{-20} \text{ m}^2$ at $\phi=0.07$ to $1.23 \times 10^{-16} \text{ m}^2$ at $\phi=0.32$ for macrofracture propagation. Our results suggest that a distributed microfracture network results in greater permeability during fluid injection in compacted mudstones ($\phi=0.07$ –0.32) in comparison to a wide macrofracture. Our modeling approach provides a simple means to estimate permeability during burial and compaction or fluid injection based on knowledge of porosity and mineralogy.

1. Introduction

Mudstone comprises 60–70% of sedimentary basin fill. During burial to 5 km, mudstone porosity (ϕ) decreases from 0.9 to 0.05, which coincides with decline in permeability (k) of up to 10 orders of magnitude [Neuzil, 1994]. These variations in permeability are important for several geological applications such as pore pressure development [Lou and Vasseur, 1992], continental slope stability

[Dugan and Flemings, 2000], hydrocarbon retention [England et al., 1987], and shale gas production [Soeder, 1988]. Accurate prediction of mudstone permeability, however, remains challenging due to factors influencing permeability such as grain dimension [Schwartz and Banavar, 1989], platelet orientation [Clennell et al., 1999], and pore geometry [Bowers and Katsube, 2002]. Clay minerals and their dimensions are often suggested as primary controls on mudstone permeability [Olsen, 1962; Dewhurst et al., 1996]. Clay platelet length ranges from 0.1 μm to 10 μm [Mondol et al., 2007] and platelets have aspect ratios (length/thickness) of 1 to 100 [Santamarina et al., 2002]. This large variation in grain dimension is suggested as the dominant controlling factor in mudstone permeability spanning 3-4 orders of magnitude for a single porosity value [Dewhurst et al., 1999a; Mondol et al., 2008].

Several models have been proposed to explain mudstone permeability. Many models assume a log-linear relationship between permeability and porosity [Rose, 1945, Nagaraj et al., 1994; Neuzil, 1994], but fail to explain the observed range of mudstone permeability for a given porosity [Yang and Aplin, 2007]. Another model used to predict mudstone permeability is the Kozeny-Carman model [Kozeny, 1927; Carman, 1937], which requires information on tortuosity, pore shape, specific pore surface area, and pore volume. While the Kozeny-Carman relationship can predict the permeability of unconsolidated mudstones with reasonable accuracy [Chapuis and Aubertin, 2003], various studies document prediction errors of several orders of magnitude [Yang and Aplin, 1998; Dewhurst et al., 1999a, b]. In other work, Yang and Aplin [2007] use pore size distribution measurements to develop an empirical power law relationship between mudstone permeability and mean pore throat radius. Several other studies utilize critical path analysis from percolation theory to predict the permeability of clay-rich samples using power-law distribution of pore sizes [Hunt and Gee, 2002; Daigle, 2016]. Thus, while several models exist to predict mudstone permeability, their application requires knowledge of pore size and tortuosity, and do not directly account for the effect of clay platelet geometry.

To improve mudstone permeability characterization, we develop a model that directly includes clay platelet geometry. We employ a three-dimensional, pore-scale model using clay platelet dimensions, pore

throat widths, platelet orientation, and porosity. We use this to evaluate the impacts of clay platelet geometry and porosity loss on permeability during burial. We estimate permeability in mudstones of homogenous and heterogenous mineralogy from lattice Boltzman simulations of water flow through mudstone pore structures and validate our results against compilation of experimental and field datasets. Finally, we extend our model to fluid injection by modifying pore structure to assess how permeability changes with growth of a microfracture network and with propagation of a macrofracture. Thus, with information on clay mineralogy, clay content, and porosity, our new approach can help estimate permeability in mudstones subjected to compaction and anthropogenic fluid injection from wastewater disposal, hydraulic fracturing, and carbon sequestration.

2. Methods

We build our mudstone models from cuboidal platelets arranged in bedding layers with each platelet oriented at an angle θ from the horizontal [Fig. 1a]. Each clay platelet has a thickness (β) and a length and width ($m\beta$), where m is the aspect ratio of the clay platelets. Pore space between particles is defined by intrabed pores of a finite width (ε) and by interbed pores of length and width (λ) [Fig. 1a]. To analyze mineralogy-specific porosity-permeability behavior of mudstones, we design three homogenous mudstone models using (1) kaolinite particles, (2) smectite particles, and (3) clay particles of intermediate size. To analyze porosity-permeability behavior of natural mudstones, we design two mudstone models of heterogenous mineralogy using smectite, illite and chlorite particles.

2.1. Homogenous Mudstone Pore Structures

In general, kaolinite particles have a length of 1- 10 μm and aspect ratios up to 25, whereas smectite particles have a length up to 0.1 μm and aspect ratios up to 100 [Mitchell and Soga, 2005]. We simulate kaolinite mudstone starting with $\phi=0.76$ ($m = 20$; $m\beta = 3 \mu\text{m}$; $\varepsilon = \lambda = 360 \text{ nm}$). We simulate smectite mudstone starting with $\phi=0.80$ ($m = 50$; $m\beta = 0.1 \mu\text{m}$; $\varepsilon = \lambda = 9 \text{ nm}$). We simulate the intermediate mudstone starting with $\phi=0.73$ ($m = 35$; $m\beta = 2 \mu\text{m}$; $\varepsilon = \lambda = 137 \text{ nm}$). Our initial mudstone porosity of

0.73-0.80 lies within range of porosity for near-seafloor mud [Daigle and Screatton, 2015; Cook and Sawyer, 2015]. Our initial pore widths of 9-360 nm are consistent with pore sizes determined from scanning electron microscopy and mercury intrusion porosimetry analyses of unconsolidated marine mudstones (1-5000 nm) [Heath, 2010], siliceous mudstones (5-750 nm) [Loucks et al., 2009], and London Clay (10-500 nm) [Dewhurst et al., 1999b].

Mineral grains are oriented randomly at deposition [Bennett et al., 1989]. In contrast, clay platelets in our model are oriented at the same angle with respect to the horizontal, θ [Fig. 1a]. Daigle and Dugan [2011] show that a porous medium with uniformly distributed grain orientations between θ_1 and θ_2 can be represented using the mean orientation angle (θ) of all grains in the matrix ($\theta = (\theta_1 + \theta_2)/2$). Clay platelet orientations can range between 0° to 90° from horizontal at deposition ($\theta_1 = 0^\circ$, $\theta_2 = 90^\circ$, $\theta = 45^\circ$) [Deamer and Kodama, 1990], therefore, we implement an initial platelet orientation of $\theta = 45^\circ$ in our homogenous mudstone models.

2.2. Heterogenous Mudstone Pore Structures

We test our modeling approach against the permeability of two natural mudstones from the Ursa Basin, Gulf of Mexico [Sawyer et al., 2009]. Sample 1324C-1H-1 is from 51.3 mbsf has a clay mineral weight fraction of 70.4%, consisting dominantly of smectite and illite [Table 1]. Sample 1324B-7H-7 is from 60.6 mbsf has a clay mineral weight fraction of 68.9%, consisting dominantly of smectite, illite, and chlorite [Table 1]. We adapt our model to include mineral weight fractions of smectite, illite, and chlorite to simulate the mudstone pore structures of samples 1324C-1H-1 and 1324B-7H-7.

We assume constant density of clay minerals. The modeled volume of each clay platelet is calculated as $m\beta \times m\beta \times \beta$. For our heterogenous mudstone models, we assume smectite platelets have an aspect ratio (m) of 50 and a length ($m\beta$) of $0.1 \mu\text{m}$, illite platelets have $m=20$ and $m\beta= 2 \mu\text{m}$ [Santamarina et al., 2012], and chlorite platelets have $m=25$ and $m\beta= 2 \mu\text{m}$ [Weber et al., 2014]. The maximum number of smectite ($no_{smectite}^{max}$), illite (no_{illite}^{max}) and chlorite ($no_{chlorite}^{max}$) platelets in each model is calculated as:

$$no_{smectite}^{max} = [0.1 \mu m * 0.1 \mu m * 0.002 \mu m] * smectite \text{ weight fraction}, \quad (1)$$

$$no_{illite}^{max} = [2 \mu m * 2 \mu m * 0.1 \mu m] * illite \text{ weight fraction}, \quad (2)$$

$$no_{chlorite}^{max} = [2 \mu m * 2 \mu m * 0.08 \mu m] * chlorite \text{ weight fraction}. \quad (3)$$

HCF is the highest common factor between $no_{smectite}^{max}$, no_{illite}^{max} and $no_{chlorite}^{max}$. The number of smectite ($no_{smectite}$), illite (no_{illite}), and chlorite ($no_{chlorite}$) platelets in each model is determined as $(no_{smectite}^{max}/HCF)$, (no_{illite}^{max}/HCF) and $(no_{chlorite}^{max}/HCF)$ respectively. The number bedding layers in each model (no_{beds}) is determined as the highest common factor between $no_{smectite}$, no_{illite} , and $no_{chlorite}$. The minimum value of no_{beds} is three. The number of smectite ($no_{smectite}^{bed}$), illite (no_{illite}^{bed}), and chlorite ($no_{chlorite}^{bed}$) platelets in each bedding layer is calculated as $(no_{smectite}/no_{beds})$, (no_{illite}/no_{beds}) , and $(no_{chlorite}/no_{beds})$ respectively. Each bedding layer is modeled with $no_{smectite}^{bed}$ smectite platelets, no_{illite}^{bed} illite platelets, and $no_{chlorite}^{bed}$ chlorite platelets, distributed randomly with intrabed pore throats of diameter ε between platelets.

The thickness of each bed (T_{bed}) is equal to the thickness of the largest platelet in the bed. For our heterogenous mudstone models *NM1* and *NM2*, the thickest platelets are illite platelets, thus $T_{bed} = 0.1 \mu m$. Each cuboidal bedding layer is initialized with $no_{smectite}^{initial}$ smectite platelets, where $no_{smectite}^{initial}$ is determined as,

$$no_{smectite}^{initial} = no_{smectite}^{bed} + \frac{[2 \mu m * 2 \mu m * 0.1 \mu m]}{[0.1 \mu m * 0.1 \mu m * 0.002 \mu m]} no_{illite}^{bed} + \frac{[2 \mu m * 2 \mu m * 0.08 \mu m]}{[0.1 \mu m * 0.1 \mu m * 0.002 \mu m]} no_{chlorite}^{bed}. \quad (4)$$

$no_{smectite}^{initial}$ represents the number of smectite platelets that equal the total volume of all platelets (smectite, illite and chlorite) in a bedding layer. Each bedding layer can consist of several tiers of smectite layers platelets [Fig. S1a]. The number of smectite tiers (t) is determined as the ratio of thickness of smectite platelets and associated interbed pore throat diameter (λ) to the thickness of each bed. In our heterogenous mudstone models *NM1* and *NM2*, $t = T_{bed} / (0.002 \mu m + \lambda)$. The initial cuboidal bedding layer is filled with $no_{smectite}^{initial}$ smectite platelets, arranged in t tiers, separated by intrabed pores of diameter λ and interbed pores of diameter ε . We then chose no_{illite}^{bed} random locations within the smectite bedding

layer and fill the simulated matrix with illite platelets of dimension $2\mu\text{m} \times 2\mu\text{m} \times 0.1\mu\text{m}$, such that the illite platelets maintain a distance of ε between platelets. Similarly, we then chose $no_{chlorite}^{bed}$ random locations within the bedding layer and fill them with chlorite platelets of dimension $2\mu\text{m} \times 2\mu\text{m} \times 0.08\mu\text{m}$, such that the chlorite platelets maintain a distance of ε with other platelets [Fig S1a]. The no_{beds} simulated beds are stacked vertically with interbed pore throat of diameter λ to develop the unrotated mudstone model [Fig. S1a, Fig. S1b]. The developed matrix is transformed by input grain orientation angle, θ , to simulate the rotated mudstone model [Fig. S1c].

To model sample 1324C-1H-1, we simulate mudstone pore structure *NM1* starting with $\phi=0.72$ consisting of 81.5% smectite and 18.5% illite. Magnetic susceptibility analyses document a range of 0° to 15° for platelet orientations at 51.3 mbsf, corresponding to the burial depth of sample 1324C-1H-1 [Yamamoto and Sawyer, 2012]. X-ray diffraction analyses reveal that degree of preferred platelet orientation at 51 mbsf is approximately double of observations at seafloor [Day-Stirrat et al., 2012]. We assume $\theta_1=0^\circ$ and $\theta_2=30^\circ$ at deposition and implement an initial platelet orientation ($\theta=(\theta_1+\theta_2)/2$) of 15° at $\phi = 0.72$ in mudstone model *NM1*.

To model sample 1324B-7H-7, we simulate mudstone pore structure *NM2* starting with $\phi=0.58$ consisting of 30.6% smectite, 41.7% illite, and 27.7% chlorite. Magnetic susceptibility analyses document a range of 0° to 12° for platelet orientations at 60.6 mbsf, corresponding to the burial depth of sample 1324B-7H-7 [Yamamoto and Sawyer, 2012]. X-ray diffraction analyses reveal that degree of preferred platelet at 60.6 mbsf is approximately double of observations at seafloor [Day-Stirrat et al., 2012]. We assume $\theta_1=0^\circ$ and $\theta_2=24^\circ$ at deposition and implement an initial platelet orientation ($\theta=(\theta_1+\theta_2)/2$) of 12° at $\phi = 0.58$ in mudstone model *NM2*.

2.3. Lattice Boltzmann Simulations

We use the open source code OpenLB [Latt, 2008] to simulate water flow through mudstone using the lattice Boltzmann method. We choose the lattice Boltzmann method because it has been used successfully

to predict the permeability of sandstones [Bosl et al., 1998], to estimate sandstone permeability from thin sections [Keehm et al., 2004], and to model the development of permeability anisotropy in mudstones [Daigle and Dugan, 2011]. We employ the single-relaxation time Bhatnagar-Gross-Krook model [Qian et al., 1992] and the D3Q19 lattice for our simulations [Martys and Chen, 1996]. Lattice Boltzmann simulations of flow yield fluid flux (q) for an applied pressure differential (ΔP); conversions between lattice Boltzmann units and SI units are made using guidelines described by Chukwodzie [2011]. For all simulations, we apply a constant pressure differential (ΔP) of 88×10^3 Pa across the model domain in the direction of flow and implement the particle bounce-back scheme [Bouzidi et al., 2001] along the orthogonal edges. Water (dynamic viscosity, $\mu_w = 8.9 \times 10^{-4}$ Pa·s; density, $\rho_w = 1000$ kg/m³) is used as the permeating fluid. By applying a constant pressure gradient in different directions, we determine vertical water flux (q_v), horizontal water flux in the plane of platelet rotation (q_{hl}) and horizontal water flux orthogonal to plane of platelet rotation (q_{h2}). In our study, we focus on horizontal water flux in the plane of platelet rotation (q_{hl}), hereafter referred to as q_h [Fig. 1a].

2.4. Calculation of Permeability and Tortuosity

We rearrange Darcy's law to calculate permeability (k) from our simulation results,

$$k = \mu_w * q * L / \Delta P, \quad (5)$$

where k is permeability (m²) and L is the length (m) over which pressure differential is applied. Vertical permeability (k_v) is calculated using water flux in the vertical direction (q_v) and horizontal permeability (k_h) is calculated using water flux in the horizontal direction (q_h). Permeability anisotropy is calculated as k_h/k_v . To ensure the applicability of Darcy's Law, we maintain Reynolds Number ($Re = (\rho_w * q * m \beta) / \mu_w$) less than 10 for all simulations. We do not consider osmotic and electrostatic effects of water flow through the simulated mudstone models, which can diminish permeability especially at low porosity conditions [Revil and Pessel, 2002].

We supplement permeability predictions with calculations of tortuosity (τ) to validate our methodology. We adapt the approach of Daigle and Dugan [2011] to calculate vertical tortuosity (τ_v) and horizontal tortuosity (τ_h) based on porosity (ϕ), platelet aspect ratio (m) and grain orientation (θ) as,

$$\tau_v = 1 + \frac{\frac{8}{9}m\cos\theta + \frac{2}{\pi}\sin\theta}{\left(\frac{3\pi}{8(1-\phi)} - \frac{1}{2}\right)} \quad \text{and} \quad (6)$$

$$\tau_h = 1 + \frac{\frac{8}{9}m\sin\theta + \frac{2}{\pi}\cos\theta}{\left(\frac{3\pi}{8(1-\phi)} - \frac{1}{2}\right)} \quad . \quad (7)$$

The average aspect ratio of platelets in our heterogenous mudstone models (*NM1* and *NM2*) is calculated as (50*smectite weight fraction + 20*illite weight fraction + 25* chlorite weight fraction). We calculate an average aspect ratio of 44.45 and 30.57 for our heterogenous mudstone models *NM1* and *NM2* respectively.

2.5. Mudstone Compaction

We simulate compaction through simultaneous decline in mudstone porosity and grain orientation [Fig. 1b]. Porosity loss during compaction is simulated through imposed, step-wise reduction of intrabed and interbed pore widths [Table S1, Table S2]. After compaction, our modeled mudstones have pore widths of 1-60 nm, which is consistent with pore throat diameters in compacted mudstones measured by X-ray diffraction and nitrogen gas-adsorption [Katsube and Williamson, 1994; Kuila and Prasad, 2012].

Natural and experimental mudstone compaction document a decline in range of observed grain orientations [Day-Stirrat et al., 2012] and an increase in horizontal bedding character [Aplin et al., 2006]. During compaction of our homogenous mudstone models we assume a decline in θ_2 from 90° to 0° and $\theta_1=0^\circ$. We implement a compaction orientation function in our homogenous mudstone models through the prescribed decline in representative platelet orientation ($\theta = (\theta_1+\theta_2)/2$) from 45° to 0° [Table S1].

Day-Stirrat et al. [2012] document a decline in range of platelet orientations with consolidation at IODP Site 1324, with an increase in preferred horizontal orientation. Based on this, we assume θ_2 approaches 0° during compaction in the *NM1* mudstone model ($\theta_1=0^\circ$ and $\theta_2=30^\circ$ at deposition). Thus, we simulate

compaction of mudstone model *NM1* with uniform representative grain orientation ($\theta = (\theta_1 + \theta_2)/2$) declining from $\theta = 15^\circ$ at $\phi = 0.72$ to $\theta = 0^\circ$ at $\phi = 0.32$ [Table S2]. Similarly, we assume θ_2 approaches 0° during compaction in the *NM2* mudstone model ($\theta_1 = 0^\circ$ and $\theta_2 = 24^\circ$ at deposition). Thus, we simulate compaction of mudstone model *NM2* with uniform representative grain orientation ($\theta = (\theta_1 + \theta_2)/2$) decreasing from $\theta = 12^\circ$ at $\phi = 0.58$ to $\theta = 0^\circ$ at $\phi = 0.25$ [Table S2].

In general, the modeled compaction orientation function replicates the increase in horizontal bedding character during compaction in mudstones, observed during natural and experimental compaction. We simulate faster decline in platelet orientation angle at high porosity states in our models [Table S1; Table S2], consistent with experimental mudstone compaction [Dewhurst et al., 1999a]. Vertical and horizontal permeability is calculated during the step-wise compaction of mudstone models [Table S1; Table S2].

3. Compaction Model Results

In our kaolinite compaction model, k_v decreases from $8.31 \times 10^{-15} \text{ m}^2$ at $\phi = 0.76$ to $6.33 \times 10^{-19} \text{ m}^2$ at $\phi = 0.14$ [Fig. 2], following a log-linear trend ($R^2 = 0.99$),

$$\log(k_v^{kaolinite}) = 6.48 \phi - 18.86 . \quad (8)$$

Simultaneously, k_h decreases from $1.01 \times 10^{-14} \text{ m}^2$ to $1.43 \times 10^{-17} \text{ m}^2$ [Table S1] and k_h/k_v increases from 1.32 to 22.6 [Fig. 3]. The reduction in vertical permeability during compaction is accompanied by an increase in vertical tortuosity from 3.98 to 21.64 [Fig. S2a] and a decrease in horizontal tortuosity from 3.98 to 1.74 [Table S1].

In our smectite compaction model, k_v decreases from $6.48 \times 10^{-17} \text{ m}^2$ at $\phi = 0.80$ to $1.30 \times 10^{-23} \text{ m}^2$ at $\phi = 0.16$ [Fig. 2], following a log-linear trend ($R^2 = 0.99$),

$$\log(k_v^{smectite}) = 10.59 \phi - 24.44 . \quad (9)$$

Simultaneously, k_h decreases from $1.33 \times 10^{-16} \text{ m}^2$ to $9.35 \times 10^{-22} \text{ m}^2$ [Table S1] and k_h/k_v increases from 1.94 to 71.9 [Fig. 3]. The reduction in vertical permeability during compaction is accompanied by an increase

in vertical tortuosity from 7.08 to 50.65 [Fig. S2a] and a decrease in horizontal tortuosity from 7.08 to 1.71 [Table S1].

In our intermediate mudstone compaction model, k_v decreases from $6.10 \times 10^{-16} \text{ m}^2$ at $\phi = 0.73$ to $1.02 \times 10^{-20} \text{ m}^2$ at $\phi = 0.07$ [Fig. 2], following a log-linear trend ($R^2 = 0.98$),

$$\log(k_v^{int}) = 6.73 \phi - 20.16 . \quad (10)$$

Simultaneously, k_h decreases from $1.11 \times 10^{-15} \text{ m}^2$ to $4.68 \times 10^{-19} \text{ m}^2$ [Table S1] and k_h/k_v increases from 1.82 to 45.6 [Fig. 3]. The reduction in vertical permeability during compaction is accompanied by an increase in vertical tortuosity from 6.72 to 41.61 [Fig. S2a] and a decrease in horizontal tortuosity from 6.72 to 1.83 [Table S1].

In our *NM1* compaction model (designed after sample 1324C-1H-1), k_v decreases from $1.54 \times 10^{-16} \text{ m}^2$ at $\phi = 0.72$ ($\theta = 15^\circ$) to $7.09 \times 10^{-21} \text{ m}^2$ at $\phi = 0.32$ ($\theta = 0^\circ$) [Fig. 4], following a log-linear trend ($R^2 = 0.99$),

$$\log(k_v^{NM1}) = 10.93 \phi - 23.63 . \quad (11)$$

Simultaneously, k_h decreases from $1.39 \times 10^{-15} \text{ m}^2$ to $2.66 \times 10^{-19} \text{ m}^2$ [Table S2] and k_h/k_v increases from 8.97 to 37.59 [Fig. 3]. The reduction in vertical permeability during compaction is accompanied by an increase in vertical tortuosity from 11.30 to 32.95 [Fig. S2b] and a decrease in horizontal tortuosity from 3.91 to 1.52 [Table S2].

In our *NM2* compaction model (designed after sample 1324B-7H-7), k_v decreases from $3.11 \times 10^{-17} \text{ m}^2$ at $\phi = 0.58$ ($\theta = 12^\circ$) to $4.79 \times 10^{-20} \text{ m}^2$ at $\phi = 0.25$ ($\theta = 0^\circ$) [Fig. 4], following a log-linear trend ($R^2 = 0.99$),

$$\log(k_v^{NM2}) = 8.28 \phi - 21.32 . \quad (12)$$

Simultaneously, k_h decreases from $2.27 \times 10^{-16} \text{ m}^2$ to $1.51 \times 10^{-18} \text{ m}^2$ [Table S2] and k_h/k_v increases from 7.29 to 31.6 [Fig. 3]. The reduction in vertical permeability during compaction is accompanied by an increase in vertical tortuosity from 12.46 to 26.54 [Fig. S2b] and a decrease in horizontal tortuosity from 3.69 to 1.60 [Table S2].

The modeled decreases in k_v and k_h during compaction are due to a reduction of pore throat widths.

Greater values of k_h compared to k_v occur as interbed pores provide greater continuity in pathways for

horizontal fluid flow, while clay platelets create a more tortuous pathway for vertical flow. Vertical tortuosity increases while horizontal tortuosity decreases during compaction which amplifies permeability anisotropy [Fig. 3].

4. Discussion

4.1. Validation of Porosity-Permeability Models

We compare our modeled porosity-permeability relationships from homogenous mudstone models with experimental and field mudstone data [Mondol et al., 2008, Neuzil, 1994]. Our kaolinite and smectite models [Eq. 8,9] show good correlation (R^2 of 0.42 and 0.56) with experimental data [Fig. 2]. The modeled porosity-permeability relationships lie within range of experimental and natural mudstone datasets [Fig. 2], and the intermediate mudstone model [Eq. 10] depicts the bulk compaction-permeability behavior of mudstones [Fig. 2]. These results validate our modeling approach over representative range of grain sizes (0.1-3 μm), aspect ratios (20-50), grain orientations (45° - 0°), and porosity (0.80-0.07).

During compaction, our homogenous mudstone models document increasing permeability anisotropy from 1.32-1.94 at $\phi=0.72$ – 0.80 to 22.6–71.9 at $\phi=0.07$ – 0.16 [Fig. 3]. Experimentally determined values of anisotropy in mudstones document an increase from 1.5 to 40 during compaction [Arch and Maltman, 1990; Bhandari et al., 2015; Yang and Aplin, 2007]. Over $\phi=0.80$ – 0.16 , predictions of k_h/k_v from our mudstone models lie within range of experimentally documented mudstone anisotropy values [Fig. 3]. At porosity less than 0.16, when $\theta=0^\circ$ in our models, our smectite and intermediate mudstone models predict k_h/k_v of 71.9 and 45.6 respectively, which exceeds the range of experimental mudstone anisotropy. This overprediction of k_h/k_v is due to the simplified horizontal layering of platelets when $\theta=0^\circ$. This results in horizontally continuous interbed pores and overprediction of k_h , resulting in higher anisotropy values.

Additionally, the vertical stacking of bedding layers of disparate intrinsic permeability in our mudstone models results in amplification of permeability anisotropy [Daigle and Dugan, 2011]. Finally, natural mudstones document lower values of permeability anisotropy due to the presence of larger silt grains which are disruptive to fabric development [Schneider et al., 2011]. Since our mudstone models do not

account for the presence of larger silt particles, we calculate higher values of k_h/k_v compared to documented experimental values in natural mudstones. While the calculated k_h/k_v values lie outside experimentally observed anisotropy values, several field-scale studies infer $k_h/k_v > 100$ based on basin-scale models [Freeze and Cherry, 1979; Garven and Freeze, 1984; Bolton et al., 2000; Day-Stirrat et al., 2008]. Our models suggest that high bedding character resulting in lateral continuity of interbed pores could explain the larger k_h/k_v values inferred from analysis of natural flow systems.

Permeability data from the constant rate-of-strain consolidation experiment on sample 1324C-1H-1 document a decrease in vertical permeability from $1.08 \times 10^{-17} \text{ m}^2$ at $\phi = 0.58$ to $5.39 \times 10^{-19} \text{ m}^2$ at $\phi = 0.46$ [Long et al., 2008]. Permeability data from the constant rate-of-strain consolidation experiment on sample 1324B-7H-7 document a decrease in vertical permeability from $1.61 \times 10^{-17} \text{ m}^2$ at $\phi = 0.50$ to $3.95 \times 10^{-19} \text{ m}^2$ at $\phi = 0.33$ [Long et al., 2008]. Our modeled porosity-permeability trends for *NM1* (designed after sample 1324C-1H-1) and *NM2* (designed after 1324B-7H-7) show good agreement with experimental consolidation datasets (R^2 of 0.78 and 0.74) [Fig. 4]. In particular, the slopes of porosity-log permeability trends described by models *NM1* and *NM2* (10.93 and 8.28 respectively) are very similar to the experimental trends described samples 1324C-1H-1 and 1324B-7H-7 (10.65 and 8.16 respectively) [Long et al., 2008] [Fig. 4].

Over the range of experimentally constrained data ($\phi = 0.46 - 0.58$), Eq. 11 underestimates the permeability of sample 1324C-1H-1. While model *NM1* is simulated using clay platelets, sample 1324C-1H-1 also has 15 wt.% quartz, 8.6 wt.% plagioclase, and 6.0 wt.% calcite [Day-Stirrat et al., 2012]. Similarly, over the range of experimentally constrained data ($\phi = 0.33 - 0.50$), Eq. 12 underestimates the permeability of sample 1324B-7H-7. While model *NM2* is simulated using clay platelets, sample 1324B-7H-7 also contains 17 wt.% quartz, 9.2 wt.% plagioclase, and 4.8 wt.% calcite [John and Adate, 2009]. Our results from models *NM1* and *NM2* predict slightly lower permeability of natural samples as they do not account for the presence of sand, silt and marl, which have been shown to have a permeability-enhancing effect in mudstones [Yang and Aplin, 2010; Dewhurst et al., 1999a; Schneider et al., 2011].

However, over $\phi=0.25-0.72$ our model results exhibit good capability to predict the permeability of natural mudstones with high clay weight fraction. In addition to simulating experimental values of vertical permeability, our models also provide an estimate of horizontal permeability, permeability anisotropy, and tortuosity.

Existing experimental values for mudstone tortuosity range from 1 to 34 as porosity decreases from 0.9 to 0.05 [Boudreau and Meysmann, 2006; Arch and Maltman, 1990; Backeberg et al., 2017]. Over $\phi=0.16 - 0.8$, we calculate values of τ_v and τ_h ranging from 1.52 to 32.95 [Table S1; Table S2], which lies within range of reported tortuosity values. At porosity less than 0.16, when $\theta=0^\circ$ in our models, our smectite and intermediate mudstone models predict τ_v of 50.65 and 41.61 respectively, which exceeds the range of experimental mudstone tortuosity. We calculate these larger values of τ_v at low porosity conditions due to the high aspect ratio of clay platelets in our smectite and intermediate mudstone models ($m=35-50$) and the lack of larger particles (e.g., silt) which reduce vertical tortuosity in natural mudstones by disrupting fabric development [Schneider et al., 2011; Dewhurst et al., 1996]. The increase in τ_v during compaction is accompanied by a decline in τ_h in our models [Table S1; Table S2], which is consistent with experimental observations [Dewhurst et al., 1999a]. This provides additional validation of our model approach. Thus, our methodology of simulating flow through mudstone pore structures provides a simple way to make first-order predictions of mudstone permeability based on clay composition and dimensions. We extend the developed methodology to understand the evolution of permeability during fluid injection in compacted mudstones.

4.2. Permeability During Fluid Injection in Mudstones

Anthropogenic activities such as wastewater disposal, hydraulic fracturing, and carbon sequestration involve injection of large fluid volumes into the subsurface, which can increase vertical mudstone permeability by several orders of magnitude [Soeder, 1988]. The increase in vertical permeability from fluid injection has been attributed to the growth of microfracture networks [Slatt and O'Brien, 2011] and propagation of macrofractures [Mayerhofer et al., 2006]. We extend our methodology to understand the

permeability response of compacted mudstone systems to fluid injection. The compacted, intermediate mudstone with $\phi=0.07$ and k_v of $1.02 \times 10^{-20} \text{ m}^2$ ($\theta=0^\circ$), is used as the starting model for fluid injection simulations. Using lattice Boltzmann simulations, we calculate evolution of vertical permeability for (a) growth of microfracture network [Fig. 5a] where we simulate preferential dilation of intrabed pores during fluid injection [Table S3] and (b) macrofracture propagation [Fig. 5b] where we simulate the increase in macrofracture width during fluid injection [Table S4]. In both scenarios, we simulate injection which ultimately drives a porosity increase to ~ 0.3 , representing the upper limit of dilation during fluid injection in compacted mudstones. Following the approach from our compaction models, we employed in our compaction analysis, we also evaluate the log-linear relationship between vertical permeability and porosity in mudstones during fluid injection.

As intrabed pore throats (ε^{mf}) increase from 11.42 nm to 377 nm in the microfracture network model [Fig. 5a], vertical permeability (k_v^{mf}) increases from $1.02 \times 10^{-20} \text{ m}^2$ at $\phi = 0.07$ to $2.07 \times 10^{-16} \text{ m}^2$ at $\phi = 0.29$ [Fig. 6], following the trend ($R^2 = 0.92$),

$$\log(k_v^{mf}) = 18.18 \phi - 20.58. \quad (13)$$

As the macrofracture width (ε^{frac}) increases from 11.42 nm to 2206 nm in the macrofracture propagation model [Fig. 5b], vertical permeability (k_v^{frac}) increases from $1.02 \times 10^{-20} \text{ m}^2$ at $\phi = 0.07$ to $1.23 \times 10^{-16} \text{ m}^2$ at $\phi = 0.32$ [Fig. 6], following the trend ($R^2 = 0.91$),

$$\log(k_v^{frac}) = 18.02 \phi - 21.5. \quad (14)$$

To compare the relative contribution of fracture flow to increases in mudstone permeability, we calculate the effective fracture width at each step of simulated fluid injection. Effective fracture width for growth of microfracture network (ε_{eff}^{mf}) and macrofracture propagation (ε_{eff}^{frac}) are calculated as

$$\varepsilon_{eff}^{mf} = n^{mf} * \varepsilon^{mf} - \varepsilon^i, \quad (15)$$

$$\varepsilon_{eff}^{frac} = \varepsilon^{frac} - \varepsilon^i, \quad (16)$$

where n^{mf} is the number of microfractures simulated in our model ($n^{mf}=3$) and ε^i is the pore throat width of the starting model ($\varepsilon^i=11.42$ nm). Over $\phi=0.10-0.32$, we calculate greater values of k_v^{mf} than k_v^{frac} [Fig. 6]. Simultaneously, ε_{eff}^{mf} increases from 137 nm to 1100 nm [Table S3], ε_{eff}^{frac} increases from 366 nm to 2190 nm [Table S4]. This indicates that the growth of a distributed microfracture network results in greater vertical permeability despite lower effective fracture width compared to a single macrofracture.

We assume that the modeled fracture systems are fractal in nature – macrofractures of larger width (ε^{frac}) are spaced more widely whereas microfractures of smaller width (ε^{mf}) have intergranular spacing. Our models suggest that upon fluid injection in low porosity mudstones, the growth of a distributed microfracture network yields a greater vertical mudstone permeability compared to propagation of a macrofracture. This is consistent with several experimental, numerical, and field scale studies that record greater increase in mudstone permeability upon distributed fracture growth compared to a wide macrofracture [Backeberg et al., 2017; Matthäi and Belayneh, 2004; Dahl et al., 2015]. Recent studies show that productivity of shale gas wells increases with the use of micro-proppants (1-50 μm) compared to typical proppants (100-300 μm) due to greater permeability enhancement provided by microfractures of smaller width [Calvin et al., 2017]. Thus, our modeling approach can be used to understand mudstone permeability response to fracture geometries. This predictive capability can help design injection strategies during anthropogenic activities such as hydraulic fracturing, wastewater disposal, and carbon sequestration.

5. Conclusions

We develop a simple model that predicts mudstone permeability by simulating fluid flow through pore structures using the lattice Boltzman method. We validate our model against porosity-permeability observations and extend the methodology to predict how permeability changes during fluid injection. Our model represents mudstones as an assemblage of cuboidal grains with thickness (β), aspect ratio (m),

orientation (θ) and with intrabed (ϵ) and interbed (λ) pore widths. Compaction models for three homogenous mudstones spanning the representative range of clay platelet lengths (0.1 – 3 μm) and aspect ratios (20-50) document a variation in mudstone permeability of over 3 orders of magnitude. Compaction of homogenous smectite and kaolinite models document log-linear declines in vertical permeability from $8.31 \times 10^{-15} \text{ m}^2$ – $6.84 \times 10^{-17} \text{ m}^2$ at $\phi=0.73$ - 0.80 to $6.33 \times 10^{-19} \text{ m}^2$ - $1.30 \times 10^{-23} \text{ m}^2$ at $\phi=0.14$ - 0.16, showing good correlation with experimental datasets ($R^2=0.42$ and $R^2=0.56$). Additionally, modeled trends of permeability and tortuosity from compaction of homogenous mudstone models lie within range of experimentally observed values on natural mudstones. We employ our methodology to predict the porosity-permeability character of two natural mudstones consisting of smectite, illite and chlorite platelets. Over porosity of 0.32-0.58, the porosity-permeability trends described by our heterogeneous mudstone models replicating the mineralogical composition of two natural mudstones (models *NM1* and *NM2*) show good correlation with experimental datasets ($R^2=0.78$ and $R^2=0.74$).

We extend our methodology to permeability during fluid injection in compacted mudstone due to (1) growth of a microfracture network where k_v increases from $1.02 \times 10^{-20} \text{ m}^2$ at $\phi = 0.07$ to $2.07 \times 10^{-16} \text{ m}^2$ at $\phi = 0.29$ and to (2) propagation of a macrofracture where k_v increases from $1.02 \times 10^{-20} \text{ m}^2$ at $\phi = 0.07$ to $1.23 \times 10^{-16} \text{ m}^2$ at $\phi = 0.32$. We document that a distributed microfracture network results in greater permeability in compacted mudstones ($\phi=0.07$ – 0.32) despite lower effective fracture width. In conclusion, we develop an approach to simulate mudstone permeability during compaction or fluid injection using simple inputs of clay platelet type (mineralogy), platelet geometry (thickness and aspect ratio) and pore throats (porosity). Thus, our model can be used to evaluate fluid flow in mudstone during geological processes or anthropogenic activities.

Acknowledgements: This work has been funded in part by fellowships to Harsh Biren Vora from the Department of Earth, Environment and Planetary Science, Rice University. Computing facilities were made available through the Center for Computational Geophysics. The authors benefitted from

398 discussions on numerical modeling with Dr. Julia Morgan. Modeling results and information can be
399 obtained in supporting information and at https://figshare.com/projects/LBM_Mudstone_k/58655.

References

- Aplin, A. C., I. F. Matenaar, D. K. McCarty, and B. A. van der Pluijm (2006), Influence of mechanical compaction and clay mineral diagenesis on the microfabric and pore-scale properties of deep-water Gulf of Mexico mudstones, *Clays Clay Miner.*, 54(4), 500–514, doi:10.1346/CCMN.2006.0540411.
- Aplin, A. C., Matenaar, I. F., & van der Pluijm, B. (2003). Influence of mechanical compaction and chemical diagenesis on the microfabric and fluid flow properties of Gulf of Mexico mudstones. *Journal of Geochemical Exploration*, 78, 449-451
- Arch, J., & Maltman, A. (1990). Anisotropic permeability and tortuosity in deformed wet sediments. *Journal of Geophysical Research: Solid Earth*, 95(B6), 9035-9045.
- Backeberg, N. R., F. Iacoviello, M. Rittner, T. M. Mitchell, A. P. Jones, R. Day, J. Wheeler, P. R. Shearing, P. Vermeesch, and A. Striolo (2017), Quantifying the anisotropy and tortuosity of permeable pathways in clay-rich mudstones using models based on X-ray tomography, *Sci. Rep.*, 7(1), 1–12, doi:10.1038/s41598-017-14810-1.
- Bennett, R. H., Fischer, K. M., Lavoie, D. L., Bryant, W. R., & Rezac, R. (1989). Porometry and fabric of marine clay and carbonate sediments: determinants of permeability. *Marine Geology*, 89(1-2), 127-152.
- Bhandari, A. R., P. B. Flemings, P. J. Polito, M. B. Cronin, and S. L. Bryant (2015), Anisotropy and Stress Dependence of Permeability in the Barnett Shale, *Transp. Porous Media*, 108(2), 393–411, doi:10.1007/s11242-015-0482-0.
- Bolton, A. J., A. J. Maltman, and Q. Fisher (2000), Anisotropic permeability and bimodal pore-size distributions of fine-grained marine sediments, *Mar. Petrol. Geol.*, 17, 657–672.
- Bosl, W. J., J. Dvorkin, and A. Nur (1998), A study of porosity and permeability using a lattice Boltzmann simulation, *Geophys. Res. Lett.*, 25(9), 1475–1478, doi:10.1029/98gl00859.
- Boudreau, B. P., and F. J. R. Meysman (2006), Predicted tortuosity of muds, *Geology*, 34(8), 693–696, doi:10.1130/G22771.1.
- Bouzidi, M., M. Firdaouss, and P. Lallemand (2001), Momentum transfer of a Boltzmann-lattice fluid with boundaries, *Phys. Fluids*, 13(11), 3452–3459, doi:10.1063/1.1399290.
- Bowers, G. L., and T. J. Katsube (2002), The Role of Shale Pore Structure on the Sensitivity of Wire-Line Logs to Overpressure, *Press. Regimes Sediment. Basins Their Predict. AAPG Mem.* 76, 43–60.
- Calvin, J., B. Grieser, and T. Bachman (2017), Enhancement of Well Production in the SCOOP Woodford Shale through the Application of Microproppant, *SPE Hydraul. Fract. Technol. Conf. Exhib.*, doi:10.2118/184863-MS.
- Carman, P. C. (1937). Fluid flow through granular beds. *Trans. Inst. Chem. Eng.*, 15, 150-166.

433 Chukwudozie, C. P. (2011). Pore-scale Lattice Boltzmann simulations of inertial flows in realistic porous
434 media: a first principle analysis of the forchheimer relationship.

435 Clennell, M. B., D. N. Dewhurst, K. M. Brown, and G. K. Westbrook (1999), Permeability anisotropy of
436 consolidated clays, *Muds Mudstones Phys. Fluid Flow Prop.*, 158, 79–96,
437 doi:10.1144/GSL.SP.1999.158.01.07.

438 Cook, A. E., and D. E. Sawyer (2015), The mud-sand crossover on marine seismic data, *Geophysics*,
439 80(6), A109–A114, doi:10.1190/geo2015-0291.1.

440 Dahl, J., P. Nguyen, R. Dusterhoft, J. Calvin, and S. Siddiqui (2015), Application of micro-proppant to
441 enhance well production in unconventional reservoirs: Laboratory and field results, *SPE West. Reg.*
442 *Meet. 2015 Old Horizons, New Horizons Through Enabling Technol., 2015–Janua*, 923–946.

443 Daigle, H. (2016), Application of critical path analysis for permeability prediction in natural porous
444 media, *Adv. Water Resour.*, 96, 43–54, doi:10.1016/j.advwatres.2016.06.016.

445 Daigle, H., and B. Dugan (2011), Permeability anisotropy and fabric development: A mechanistic
446 explanation, *Water Resour. Res.*, 47(12), 1–11, doi:10.1029/2011WR011110.

447 Daigle, H., and E. J. Screaton (2016), Evolution of sediment permeability during burial and subduction,
448 *Crustal Permeability*, 104–121, doi:10.1002/9781119166573.ch11.

449 Day-Stirrat, R. J., A. C. Aplin, J. Środoń, and B. A. van der Pluijm (2008), Diagenetic reorientation of
450 phyllosilicate minerals in Paleogene mudstones of the Podhale Basin, southern Poland, *Clays Clay*
451 *Miner.*, 56(1), 100–111, doi:10.1346/CCMN.2008.0560109.

452 Day-Stirrat, R. J., P. B. Flemings, Y. You, A. C. Aplin, and B. A. van der Pluijm (2012), The fabric of
453 consolidation in Gulf of Mexico mudstones, *Mar. Geol.*, 295–298, 77–85,
454 doi:10.1016/j.margeo.2011.12.003.

455 Deamer, G. A., & Kodama, K. P. (1990). Compaction-induced inclination shallowing in synthetic and
456 natural clay-rich sediments. *Journal of Geophysical Research: Solid Earth*, 95(B4), 4511–4529.

457 Dewhurst, D. N., A. C. Aplin, and J.-P. Sarda (1999b), Influence of clay fraction on pore-scale properties
458 and hydraulic conductivity of experimentally compacted mudstones, *J. Geophys. Res.*, 104, 29261,
459 doi:10.1029/1999JB900276.

460 Dewhurst, D. N., K. M. Brown, M. B. Clennell, and G. K. Westbrook (1996), A comparison of the fabric
461 and permeability anisotropy of consolidated and sheared silty clay, *Eng. Geol.*, 42(4), 253–267,
462 doi:10.1016/0013-7952(95)00089-5.

463 Dewhurst, D. N., Y. Yang, and a. C. Aplin (1999a), Permeability and fluid flow in natural mudstones,
464 *Geol. Soc. London, Spec. Publ.*, 158(1), 23–43, doi:10.1144/GSL.SP.1999.158.01.03.

465 Dugan, B. (2000), Overpressure and Fluid Flow in the New Jersey Continental Slope: Implications for
466 Slope Failure and Cold Seeps, *Science* (80-.), 289(5477), 288–291,
467 doi:10.1126/science.289.5477.288.

468 England, W. A., A. S. Mackenzie, D. M. Mann, and T. M. Quigley (1987), The movement and
 469 entrapment of petroleum fluids in the subsurface, *J. Geol. Soc. London.*, 144(2), 327–347,
 470 doi:10.1144/gsjgs.144.2.0327.

471 Fisher, M. K., C. A. Wright, B. M. Davidson, A. K. Goodwin, E. O. Fielder, W. S. Buckler, and N. P.
 472 Steinsberger (2002), Integrating Fracture Mapping Technologies to Optimize Stimulations in the
 473 Barnett Shale, *SPE Annu. Tech. Conf. Exhib.*, doi:10.2118/77441-MS.

474 Freeze, R. A., and J. A. Cherry (1979), *Groundwater*, Prentice Hall, Englewood Cliffs, N. J.

475 Garven, G., and R. A. Freeze (1984), Theoretical analysis of the role of groundwater flow in the genesis
 476 of stratabound ore deposits. 2: Quantitative results, *Am. J. Sci.*, 284, 1125–1174.

477 Heath, J. E. (2010), Multi-scale petrography and fluid dynamics of caprocks associated with geological
 478 CO₂ storage, *Dep. Earth Environ. Sci., PhD* (December), 437.

479 Hunt, A. G., and G. W. Gee (2002), Application of critical path analysis to fractal porous media:
 480 Comparison with examples from the Hanford site, *Adv. Water Resour.*, 25(2), 129–146,
 481 doi:10.1016/S0309-1708(01)00057-4.

482 Iversen, N., and B. B. Jorgensen (1993), Diffusion coefficients of sulfate and methane in marine
 483 sediment: Influence of porosity, *Geochim. Cosmochim. Acta*, 57(5), 571–578.

484 John, C. M., and T. Adatte (2009), Data report : X-ray analyses of bulk sediment in IODP Holes U1320A
 485 and U1324B , northern Gulf of Mexico, 308, doi:10.2204/iodp.proc.308.214.2009.

486 Katsube, T. J., & Williamson, M. A. (1994). Effects of diagenesis on shale nano-pore structure and
 487 implications for sealing capacity. *Clay minerals*, 29(4), 451–461.

488 Keehm, Y. (2004), Permeability prediction from thin sections: 3D reconstruction and Lattice-Boltzmann
 489 flow simulation, *Geophys. Res. Lett.*, 31(4), 3–6, doi:10.1029/2003GL018761.

490 Kozeny, J. (1927). Über kapillare leitung der wasser in boden. *Royal Academy of Science, Vienna, Proc.*
 491 *Class I*, 136, 271–306.

492 Kuila, U., and M. Prasad (2013), Specific surface area and pore-size distribution in clays and shales,
 493 *Geophys. Prospect.*, 61(2), 341–362, doi:10.1111/1365-2478.12028.

494 Latt, J. (2008), Choice of units in lattice Boltzmann simulations, *Lattice Boltzmann How tos*, (April), 1–6.

495 Long, H., P. B. Flemings, J. T. Germaine, D. M. Saffer, and B. Dugan (2008), Data report: Consolidation
 496 characteristics of sediments from IODP Expedition 308, Ursa Basin, Gulf of Mexico, *Proc. Integr.*
 497 *Ocean Drill. Progr. Sci. Results*, 308, doi:10.2204/iodp.proc.308.204.2008.

498 Loucks, R. G., R. M. Reed, S. C. Ruppel, and D. M. Jarvie (2009), Morphology, Genesis, and
 499 Distribution of Nanometer-Scale Pores in Siliceous Mudstones of the Mississippian Barnett Shale, *J.*
 500 *Sediment. Res.*, 79(12), 848–861, doi:10.2110/jsr.2009.092.

501 Lucia, F. J., Jennings Jr, J. W., Rahnis, M., & Meyer, F. O. (2001). Permeability and rock fabric from
502 wireline logs, Arab-D reservoir, Ghawar field, Saudi Arabia. *GeoArabia*, 6(4), 619-646.

503 Martys, N. S., and H. Chen (1996), Simulation of multicomponent fluids in complex three-dimensional
504 geometries by the lattice Boltzmann method, *Phys. Rev. E - Stat. Physics, Plasmas, Fluids, Relat.*
505 *Interdiscip. Top.*, 53(1), 743–750, doi:10.1103/PhysRevE.53.743.

506 Matthäi, S. K., and M. Belayneh (2004), Fluid flow partitioning between fractures and a permeable rock
507 matrix, *Geophys. Res. Lett.*, 31(7), 1–5, doi:10.1029/2003GL019027.

508 Mayerhofer, M. J., E. P. Lolon, J. E. Youngblood, and J. R. Heinze (2006), Integration of Microseismic-
509 Fracture-Mapping Results with Numerical Fracture Network Production Modeling in the Barnett
510 Shale, *SPE Annu. Tech. Conf. Exhib.*, doi:10.2118/102103-MS.

511 Mitchell, J. K., & Soga, K. (2005). *Fundamentals of soil behavior* (Vol. 3). New York: John Wiley &
512 Sons.

513 Mondol, N. H., Bjørlykke, K., & Jahren, J. (2008). Experimental compaction of clays: Relationship
514 between permeability and petrophysical properties in mudstones. *Petroleum Geoscience*, 14(4), 319-
515 337.

516 Mondol, N. H., K. Bjørlykke, J. Jahren, and K. Høeg (2007), Experimental mechanical compaction of
517 clay mineral aggregates-Changes in physical properties of mudstones during burial, *Mar. Pet. Geol.*,
518 24(5), 289–311, doi:10.1016/j.marpetgeo.2007.03.006.

519 Nagaraj, T. S. (1994). Stress state permeability relationships for overconsolidated clays. *Geotechnique*,
520 44(2), 349-352.

521 Neuzil, C. E. (1994). How permeable are clays and shales?. *Water resources research*, 30(2), 145-150.

522 Olsen, H. W. (1960), Hydraulic Flow Through Saturated Clays, *Clays Clay Miner.*, 9(1), 131–161,
523 doi:10.1346/CCMN.1960.0090108.

524 Qian, Y. H., D. D’Humières, and P. Lallemand (1992), Lattice BGK Models for Navier-Stokes Equation,
525 *Europhys. Lett.*, 17(6BIS), 479–484, doi:10.1209/0295-5075/17/6/001.

526 Revil, A., and M. Pessel (2002), Electroosmotic flow and the validity of the classical Darcy equation in
527 silty shales, *Geophys. Res. Lett.*, 29(9), 14-1-14–4, doi:10.1029/2001gl013480., and M. Pessel
528 (2002), Electroosmotic flow and the validity of the classical Darcy equation in silty shales, *Geophys.*
529 *Res. Lett.*, 29(9), 14-1-14–4, doi:10.1029/2001gl013480.

530 Rose, H. E. (1945). An investigation into the laws of flow of fluids through beds of granular materials.
531 *Proceedings of the Institution of Mechanical Engineers*, 153(1), 141-148.

532 Santamarina, J. C., K. A. Klein, Y. H. Wang, and E. Prencke (2002), Specific surface: determination and
533 relevance, *Can. Geotech. J.*, 39(1), 233–241, doi:10.1139/t01-077.

- 534 Sawyer, D. E., R. Jacoby, P. Flemings, and J. T. Germaine (2008), Data report : particle size analysis of
535 sediments in the Ursa Basin , IODP Expedition 308 Sites U1324 and U1322 , northern Gulf of
536 Mexico, 308, 1–20, doi:10.2204/iodp.proc.308.205.2008.
- 537 Schneider, J., P. B. Flemings, R. J. Day-Stirrat, and J. T. Germaine (2011), Insights into pore-scale
538 controls on mudstone permeability through resedimentation experiments, *Geology*, 39(11), 1011–
539 1014, doi:10.1130/G32475.1.
- 540 Schwartz, L. M., and J. R. Banavar (1989), Transport properties of disordered continuum systems, *Phys.*
541 *Rev. B*, 39(16), 11965–11970, doi:10.1103/PhysRevB.39.11965.
- 542 Slatt, R. M., and N. R. O’Brien (2011), Pore types in the Barnett and Woodford gas shales: Contribution
543 to understanding gas storage and migration pathways in fine-grained rocks, *Am. Assoc. Pet. Geol.*
544 *Bull.*, 95(12), 2017–2030, doi:10.1306/0330110145.
- 545 Soeder, D. J. (1988). Porosity and permeability of eastern Devonian gas shale. *SPE Formation*
546 *Evaluation*, 3(01), 116-124.
- 547 Weber, C., M. Heuser, and H. Stanjek (2014), A collection of aspect ratios of common clay minerals
548 determined from conductometric titrations, *Clay Miner.*, 49(3), 495–498,
549 doi:10.1180/claymin.2014.049.3.10.
- 550 Xiaorong Luo, and G. Vasseur (1992), Contributions of compaction and aquathermal pressuring to
551 geopressure and the influence of environmental conditions, *Am. Assoc. Pet. Geol. Bull.*, 76(10),
552 1550–1559, doi:10.1306/BDFF8FB0-1718-11D7-8645000102C1865D.
- 553 Yamamoto, Y., & Sawyer, D. E. (2012). Systematic Spatial Variations in the Fabric and Physical
554 Properties of Mass-Transport Deposits in the Ursa Region, Northern Gulf of Mexico. In *Submarine*
555 *Mass Movements and Their Consequences* (pp. 649-658). Springer, Dordrecht.
- 556 Yang, Y., and A. C. Aplin (1998), Influence of lithology and compaction on the pore size distribution and
557 modelled permeability of some mudstones from the Norwegian margin, *Mar. Pet. Geol.*, 15(2), 163–
558 175, doi:10.1016/S0264-8172(98)00008-7.
- 559 Yang, Y., and A. C. Aplin (2007), Permeability and petrophysical properties of 30 natural mudstones, *J.*
560 *Geophys. Res. Solid Earth*, 112(3), doi:10.1029/2005JB004243.
- 561 Yang, Y., and A. C. Aplin (2010), A permeability-porosity relationship for mudstones, *Mar. Pet. Geol.*,
562 27(8), 1692–1697, doi:10.1016/j.marpetgeo.2009.07.001.

Table 1: Clay mineralogy of reference samples for mudstone porosity-permeability behavior. Data from Long et al. [2008], Sawyer et al. [2009] and Day-Stirrat et al. [2012].

	Sample: 1324C-1H-1	Sample: 1324B-7H-7
Core Top (mbsf)	51.1	60.3
Initial Porosity	0.59	0.51
Clay Mineral Fraction (wt. %)	70.4	68.9
Smectite (wt. %)	82.1	27.3
Illite (wt. %)	17.9	38.8
Chlorite (wt. %)	Trace	25.0
Quartz (wt. %)	Trace	8.8
Consolidation Experiment	CRS 799	CRS 015B

Figure Captions

Figure 1: (a) Schematic of initial mudstone structure built from clay platelets (grey cuboids) using inputs of platelet thickness (β) and aspect ratio (m) and intrabed (ε) and interbed (λ) pore throat widths and orientation angle with respect to horizontal (θ). Flux of fluid in vertical and horizontal direction are represented by q_v and q_h respectively. (b) Mudstone structure after compaction simulated by reduction in pore throat widths, ε and λ , and platelet orientation angle (θ).

Figure 2: Porosity-vertical permeability model results (symbols) and best-fit lines during compaction for kaolinite, smectite, and intermediate mudstone models. Modeled porosity-permeability trends show good correlation with natural and experimental mudstone permeability compilation [Neuzil, 1994] and experimental data on kaolinite and smectite [Mondol et al., 2008].

Figure 3: Permeability anisotropy (k_h/k_v) exhibits an inverse correlation with porosity (ϕ) and platelet size ($m\beta$) during compaction of homogenous kaolinite, smectite and intermediate mudstone models, and heterogenous NM1 (designed after sample 1324C-1H-1) and NM2 (designed after sample 1324B-7H-7) models.

Figure 4: Porosity-permeability predictions (symbols) and best-fit lines during compaction of heterogenous mudstone models *NM1* (designed after sample 1324C-1H-1) and *NM2* (designed after sample 1324B-7H-7). Modeled porosity-permeability trends of *NM1* and *NM2* lie within range of mudstone permeability compilation [Neuzil, 1994], and show good correlation with experimental data on natural mudstones 1324C-1H-1 (Experiment CRS799) and 1324B-7H-7 (Experiment CRS015B) respectively [Long et al., 2008].

Figure 5: (a) Schematic of a microfracture network in compacted intermediate mudstone model during fluid injection. In our model microfracture width increases from 11.42 nm to 377 nm [Table S3] (b) Schematic of macrofracture through compacted intermediate mudstone model during fluid injection. In our model, macrofracture width increases from 11.42 nm to 2206 nm [Table S4].

Figure 6: Porosity-vertical permeability model predictions (symbols) and best-fit lines during fluid injection accommodated through prescribed growth of microfracture network or propagation of a macrofracture. For $\phi=0.07-0.32$, growth of microfracture network (k_v^{mf}) results in greater permeability increase than macrofracture propagation (k_v^{frac}). Mudstone permeability compilation [Neuzil, 1994] shown for reference.

Figure 1.

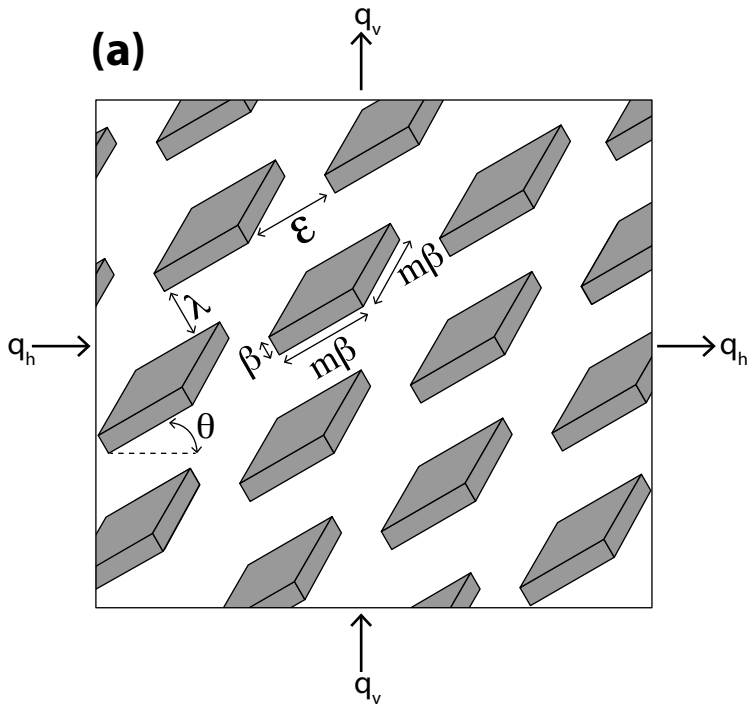
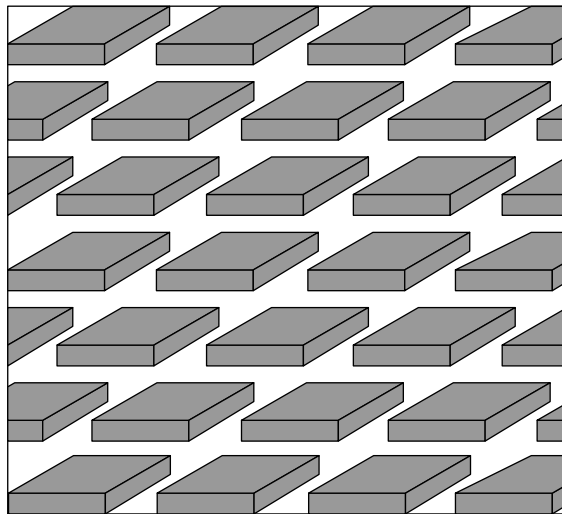
(a)**(b)**

Figure 2.

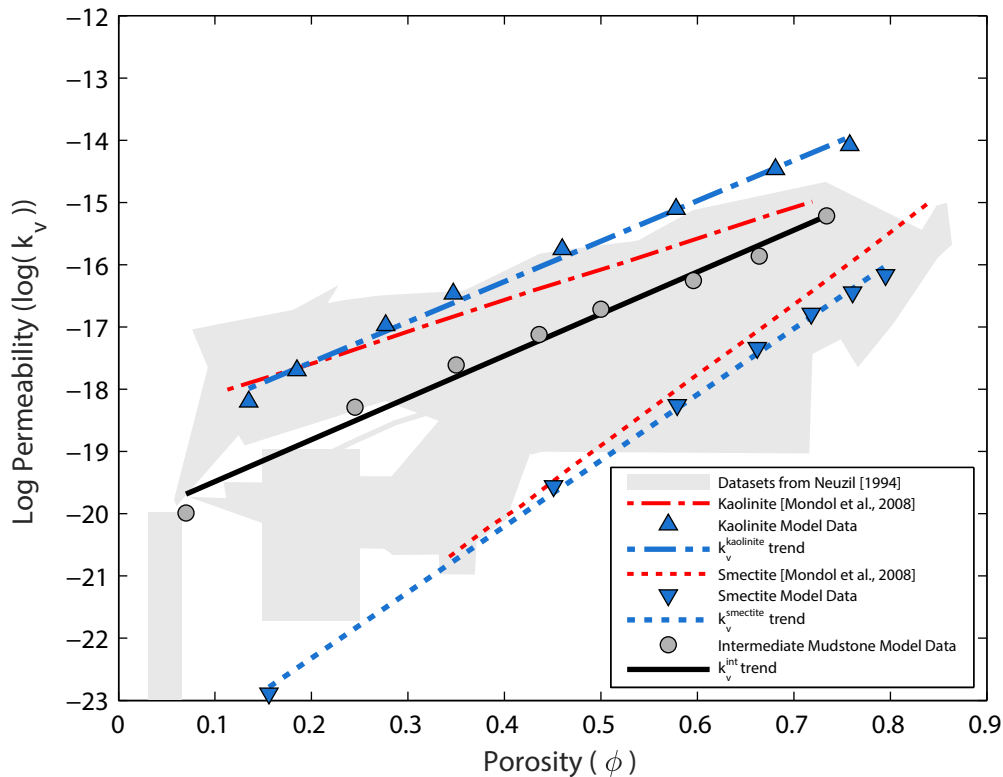


Figure 3.

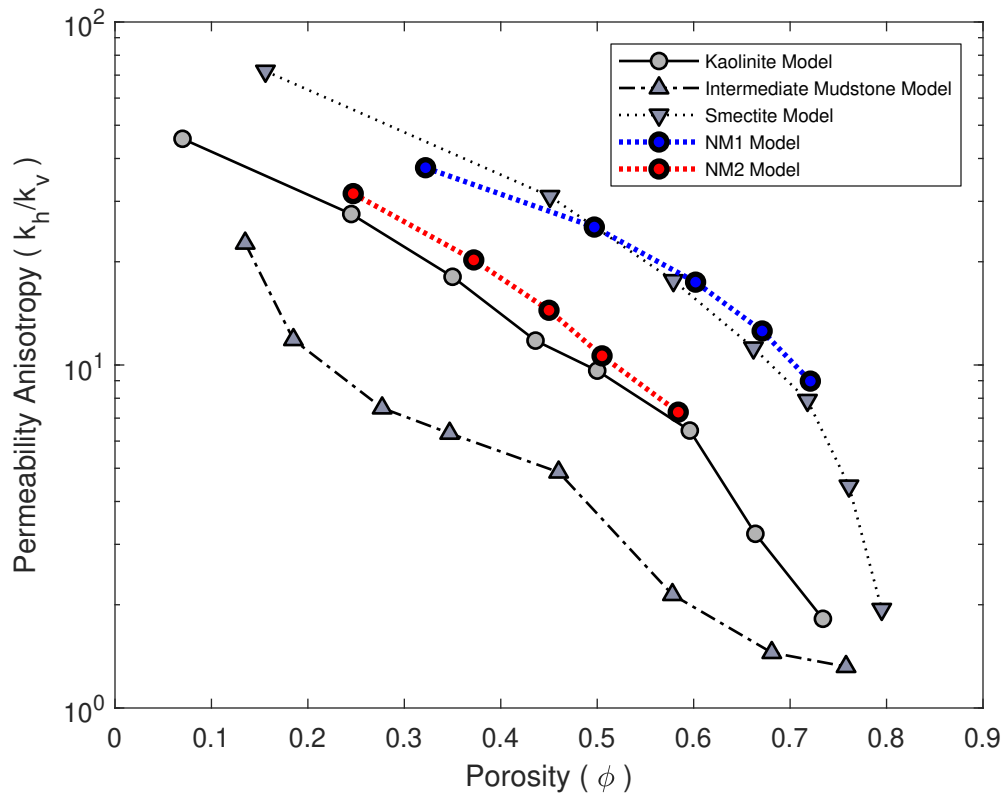


Figure 4.

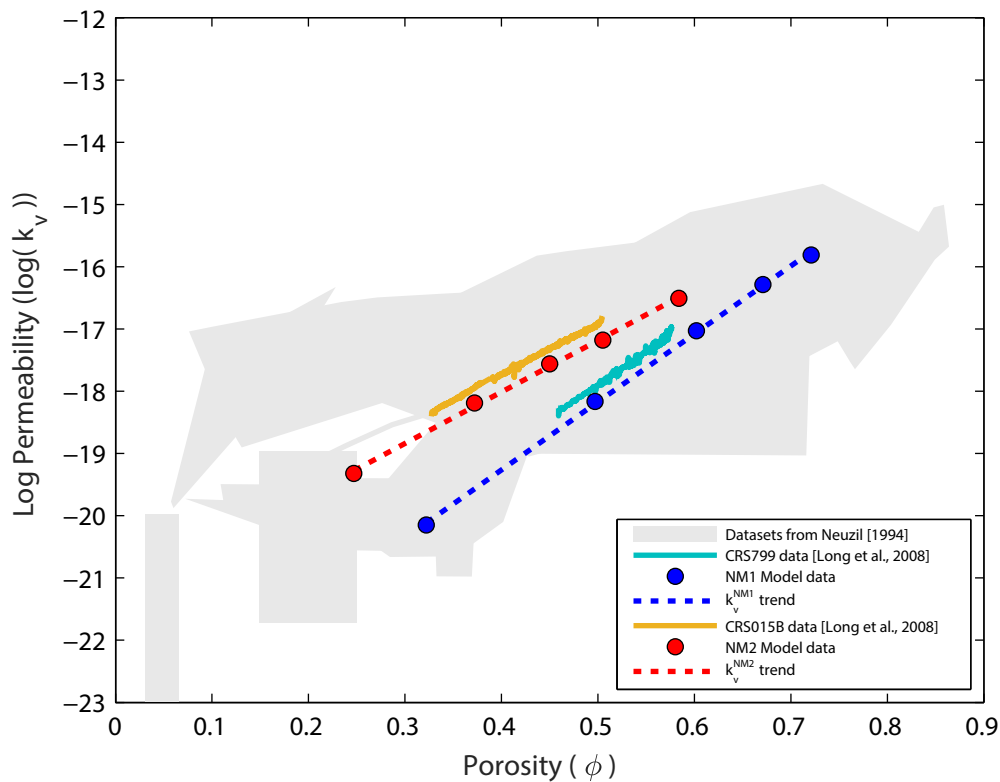


Figure 5.

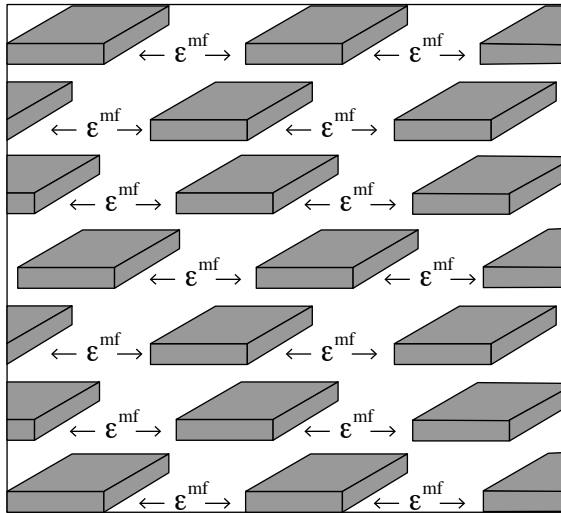
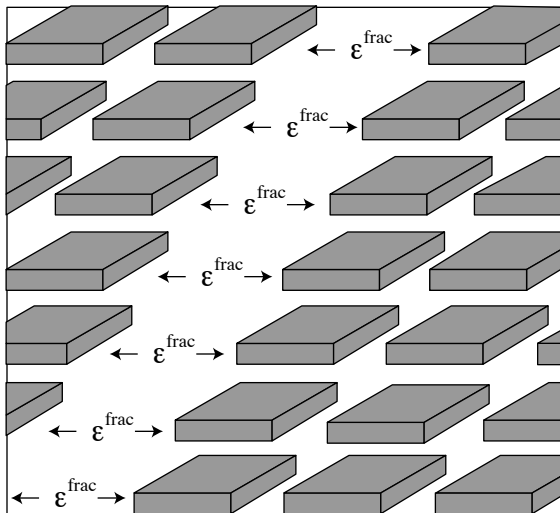
(a)**(b)**

Figure 6.

